A Dual-Frequency Dual-Channel WPT System With Wide Range ZVS and Communication-Free Capability

Jingchi Wu, Linghui Meng, Yuhao Deng, Youshong Zhou, Jiangpeng Yang, Shun Wang, Siyang Liu, and Zeliang Shu, *Senior Member, IEEE*

***Abstract*—Achieving efficient power regulation without communication in wireless power transfer (WPT) systems remains a significant challenge, particularly under varying load and coupling conditions. This article proposes a dual-frequency dual-channel WPT system by introducing a third harmonic resonant channel alongside the fundamental power channel. The third harmonic current serves multiple roles: it enables communication-free synchronization via implicit phase feedback, contributes actively to power transfer, and extends the zero-voltage switching (ZVS) range of the primary-side inverter without increasing the switching frequency. A two-stage synchronous control strategy is developed to regulate power based solely on local measurements, avoiding complex sensing, parameters estimation, or digital modulation-demodulation. To control the overall size of the coupler, a compact coil design is adopted, while maintaining a competitive power density. The proposed system is validated on a 1.7 kW experimental platform. Results confirm the system's wide ZVS range and its ability to maintain stable control without communication. The system achieves a peak efficiency of 94.39%, and remains above 93.5% when the output power exceeds 50% .**

***Index Terms*—Dual-channel, harmonic current, wireless power transfer without communication, zero-voltage switching (ZVS).**

I. Introduction

MAGNETIC resonance wireless power transfer (WPT) systems offer advantages such as isolated power transfer, low maintenance costs, misalignment tolerance, and high flexibility [1], [2], [3]. However, to ensure charging profiles that meet the high-performance standards of lithium-ion batteries, constant current (CC), constant voltage (CV), and constant power (CP) charging are required to accommodate various application scenarios, such as misaligned coils and dynamic battery charging [4], [5].

In [6] and [7], the Bluetooth/Wi-Fi wireless devices are widely used for power control communication to ensure physical separation between the primary and secondary sides. It may cause cost increasing, signal delay, susceptibility to interference.

To achieve wireless power control without additional communication devices, existing literature mainly proposes four approaches. The first method utilizes topology-based, load-independent outputs [8], [9], [10], providing CV or CC output at the receiver. However, it lacks direct transmitter-side power adjustability, limiting control flexibility. The second method estimates transmitted power through reflected impedance theory and parameters identification of load and mutual inductance [4], [11], [12]. This approach requires real-time primary-side voltage and current measurements, and its accuracy can be sensitive to coupling variations and system nonlinearities. The third method incorporates an additional dc–dc converter at the receiver side for local power regulation [13], [14]. Despite offering convenient local control, this approach adds complexity, increases cost, and introduces additional losses. Finally, the fourth approach transmits control signals via high-speed analog to digital or digital to analog conversion, or signal modulation-demodulation through the power channel itself [15], [16], [17], [18]. These methods enable information synchronization and effective power regulation without extra communication modules, but they may increase system complexity and introduce interference between power and information, as both share the same channel, especially under dynamic load or coupling conditions.

Moreover, achieving zero-voltage switching (ZVS) in the primary-side full-bridge inverter under phase-shift modulation remains challenging, particularly at low duty cycles, which significantly reduces system efficiency. Several methods have been proposed to achieve full ZVS operation and effective power regulation. In [19], switch-controlled capacitors are employed to enhance the power factor and control output power, achieving ZVS for the auxiliary switches. However, this method involves complex control strategies and a complicated hardware implementation. Pulse density modulation (PDM) has also been applied as a simple method to achieve wide-range ZVS [20]. A hybrid modulation method on the primary side is presented in [21], which enables wide-range voltage regulation and partial

---

Received 6 April 2025; revised 28 May 2025 and 30 June 2025; accepted 8 August 2025. Date of publication 1 September 2025; date of current version 13 November 2025. This work was supported in part by the National Natural Science Foundation of China under Grant 52577217, in part by Chengdu Municipal Science and Technology Program under Grant 2024-YF05-00673-SN, and in part by Doctoral Innovation Fund Program of Southwest Jiaotong University under Grant CX-2025ZD02. Recommended for publication by Associate Editor K. Joshi. *(Corresponding author: Zeliang Shu.)*

The authors are with the School of Electrical Engineering, Southwest Jiaotong University, Chengdu 610097, China (e-mail: jingchiwu@my.swjtu.edu.cn; mailtolinghui@my.swjtu.edu.cn; yh_deng@my.swjtu.edu.cn; zhouys@my.swjtu.edu.cn; yjp_pe@my.swjtu.edu.cn; wangshun@my.swjtu.edu.cn; siyangliu@my.swjtu.edu.cn; shuzeliang@swjtu.edu.cn).

Color versions of one or more figures in this article are available at https://doi.org/10.1109/TPEL.2025.3599238.

Digital Object Identifier 10.1109/TPEL.2025.3599238

ZVS operation. However, in [19], [20], and [21], the ZVS current is close to zero. As a result, the presence of parasitic capacitance in the switches leads to incomplete ZVS in practical applications. Overall, existing research on power control in WPT systems is limited by communication dependencies, auxiliary device complexity, and efficiency challenges.

In recent years, multifrequency WPT systems have attracted growing attention. In [22], a multifrequency WPT system was developed to support multiload applications, with each channel operating independently. In [23], a decoupled multichannel WPT system based on multilevel inverters was proposed, where each channel operates at a different frequency to enable independent control. However, the generation of multiple frequencies requires a large number of switching devices and capacitors. Additionally, some recent works [24], [25] have explored the application of the second harmonic, which is typically generated passively through rectification effects, as a feedback signal in low-power RF WPT systems, primarily for positioning or backscatter communication. However, these systems usually require precise filtering and complex feedback paths, and are less suited for medium/high-power inductive WPT applications. In contrast, the third harmonic current has a relatively high amplitude and can be easily extracted from the fundamental square-wave excitation through resonant filtering. In [26], [27], and [28], hybrid dual-frequency WPT systems based on the first and third harmonic current transmission were proposed to achieve constant voltage output and higher efficiency under coupler misalignment, leveraging the high-frequency characteristics of the third harmonic. In [29], a hybrid first and third harmonic current WPT system was presented to achieve smooth power variation across a wide coupling range. These studies commonly rely on the band-pass characteristic of each resonant channel to achieve interchannel isolation. The third harmonic channel operates independently from the fundamental power channel, enabling communication-free control and partial power transfer without interference. Moreover, since the voltage feedback information can be converted to the phase of the third harmonic current, which shares the same path as the third harmonic power transfer, the phase information can be easily extracted by the primary side. Additionally, through proper design, the third harmonic current can improve the ZVS conditions of the inverter.

Based on the characteristics of the third harmonic, this article proposes a novel fundamental and third-harmonic dual-channel wireless power transfer (F3HDC-WPT) system, which enables communication-free power control and achieves wide-range ZVS. Compared to existing studies, the proposed F3HDC-WPT system offers the following key advantages.

1) *Communication-Free Functionality:* The third harmonic channel, operating independently from the fundamental channel, simultaneously transmits power, and phase information feedback, eliminating the need for external communication devices or increasing the switching frequency.
2) *Enhanced ZVS Performance:* The third harmonic current extends the ZVS operating range, effectively improving efficiency, especially under low-power operating conditions.

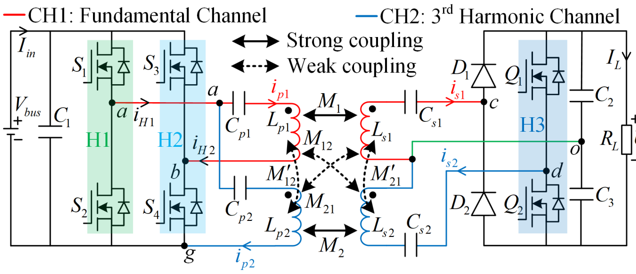

Fig. 1. Topology of proposed F3HDC-WPT system.

3) A control strategy is developed for the proposed system, enabling closed-loop power control under varying load and coupling conditions. It eliminates the need for complex sensing, real-time computation, and avoids interference between power transfer and signal communication.

To ensure the effectiveness of the proposed F3HDC-WPT system, several design requirements must be considered.

1) The secondary side coils should have dimensions similar to the primary side coils. This helps maintain a relatively constant ratio of M_2/M_1 under misalignment, ensuring reliable closed-loop control and wide-range ZVS.
2) The weak interchannel coupling should be minimized through proper arrangement of the coils.
3) The harmonic channel should be designed with a relatively large self-inductance to provide sufficient filtering capability for suppressing nonthree-order harmonics.

II. TOPOLOGY, MODULATION, AND CONTROLLER DESIGN

A. *Proposed Dual Resonant Tank WPT Topology*

The topology of the proposed F3HDC-WPT system is illustrated in Fig. 1. It comprises two series–series (S–S) resonant channels: the fundamental resonant channel (CH1), formed by L_{p1}, C_{p1}, L_{s1}, and C_{s1}, and the third-harmonic resonant channel (CH2), consisting of L_{p2}, C_{p2}, L_{s2}, and C_{s2}.

On the primary side, CH1 is driven by a full bridge (FB) inverter composed of switches S_1–S_4, which form two bridge arms, H1 and H2. CH2 is connected between the midpoint of H1 (shared with CH1) and the ground point g, resulting in i_{H1} being the sum of i_{p1} and i_{p2}. On the secondary side, CH1 is connected to a half-bridge rectifier (D_1, D_2), while CH2 is connected to an active rectifier half-bridge (H3) consisting of switches Q_1 and Q_2. The system outputs a dc voltage U_o.

The mutual inductance parameters include M_1 and M_2 for individual channels, while M_{12}, M'_{12}, M_{21}, and M'_{21} represent the weak interchannel coupling inductances.

The port voltages of FB and H1 are square waves [30], and can be expressed as follows:

$$u_{ab} = \sum_{n=1}^{\infty} \frac{4V_{\text{bus}} \sin(n\pi D)}{n\pi} \cdot \sin\left[n\omega_1 t + \frac{\pi(1-2nD)}{2}\right] \quad (1)$$

$$u_{ag} = \frac{V_{\text{bus}}}{2} + \sum_{n=1}^{\infty} \frac{2V_{\text{bus}}}{n\pi} \cdot \sin(n\omega_1 t) \quad (2)$$

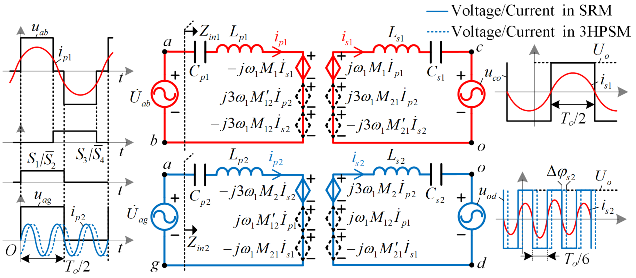

Fig. 2. Equivalent circuit of proposed F3HDC-WPT system.

where D is the duty cycle ($0 \leq D \leq 0.5$), n represents the odd order ($n = 1, 3, 5, \cdots$), and $\omega_1 = 2\pi f_o = 2\pi/T_o$ is the fundamental angular frequency; where f_o is the fundamental frequency and T_o is the corresponding period. According to (1) and (2), the amplitude of higher-order harmonics decreases as n increases.

To configure CH1 as the fundamental channel and CH2 as the third harmonic channel, the resonant parameters are as follows:

$$\begin{cases} C_{p1} = \frac{1}{\omega_1^2 L_{p1}}, C_{p2} = \frac{1}{(3\omega_1)^2 L_{p2}} \\ C_{s1} = \frac{1}{\omega_1^2 L_{s1}}, C_{s2} = \frac{1}{(3\omega_1)^2 L_{s2}}. \end{cases} \tag{3}$$

Applying (3), CH1 and CH2 act as band-pass filters for the fundamental and third harmonics, respectively. Consequently, CH1 primarily contains the fundamental harmonic, while CH2 exclusively transmits the third harmonic current, eliminating the need for the tripling switching frequency for the inverter. As shown in Fig. 2, the load can be equivalently represented as a voltage source with the same frequency as the current of the corresponding channel. For weak coupling impact, the induced voltages caused by M_{12}, M'_{12}, M_{21}, and M'_{21} are as follows:

$$\begin{aligned} \dot{U}_{\Delta p1} &= j3\omega_1 M'_{12} \dot{I}_{p2} - j3\omega_1 M_{12} \dot{I}_{s2}; \dot{U}_{\Delta p2} \\ &= j\omega_1 M'_{12} \dot{I}_{p1} - j\omega_1 M_{12} \dot{I}_{s1} \\ \dot{U}_{\Delta s1} &= j3\omega_1 M_{21} \dot{I}_{p2} - j3\omega_1 M'_{21} \dot{I}_{s2}; \dot{U}_{\Delta s2} \\ &= j\omega_1 M_{12} \dot{I}_{p1} - j\omega_1 M'_{21} \dot{I}_{s1}. \end{aligned} \tag{4}$$

For CH1, the weak coupling induced voltages, $U_{\Delta p1}$ and $U_{\Delta s1}$, primarily consist of third-harmonic components, whereas $U_{\Delta p2}$ and $U_{\Delta s2}$ are predominantly composed of first harmonic components. The resulting effects on the currents can be expressed as follows:

$$\begin{cases} \dot{I}_{\Delta p1} = \frac{j3\omega_1 M'_{12} \dot{I}_{p2} - j3\omega_1 M_{12} \dot{I}_{s2}}{j3\omega_1 L_{p1} + 1/(j3\omega_1 C_{p1})} = \frac{9M'_{12} \dot{I}_{p2} - 9M_{12} \dot{I}_{s2}}{8L_{p1}} \\ \dot{I}_{\Delta p2} = \frac{j\omega_1 M'_{12} \dot{I}_{p1} - j\omega_1 M_{12} \dot{I}_{s1}}{j\omega_1 L_{p2} + 1/(j\omega_1 C_{p2})} = \frac{M_{12} \dot{I}_{s1} - M'_{12} \dot{I}_{p1}}{8L_{p2}} \\ \dot{I}_{\Delta s1} = \frac{j3\omega_1 M_{21} \dot{I}_{p2} - j3\omega_1 M'_{21} \dot{I}_{s2}}{j3\omega_1 L_{s1} + 1/(j3\omega_1 C_{s1})} = \frac{9M_{21} \dot{I}_{p2} - 9M'_{21} \dot{I}_{s2}}{8L_{s1}} \\ \dot{I}_{\Delta s2} = \frac{j\omega_1 M_{12} \dot{I}_{p1} - j\omega_1 M'_{21} \dot{I}_{s1}}{j\omega_1 L_{s2} + 1/(j\omega_1 C_{s1})} = \frac{M'_{21} \dot{I}_{s1} - M_{12} \dot{I}_{p1}}{8L_{s2}}. \end{cases} \tag{5}$$

Fig. 3 shows the simulated total harmonic distortion (THD) of the operating currents in CH1 and CH2 under varying weak coupling inductance values. The simulation is conducted using MATLAB/Simulink. The system is configured with self-inductance parameters: $L_{p1} = L_{s1} = 130\,\mu$H, $L_{p2} = L_{s2} =$ 80 μH. As observed, when the weak interchannel coupling inductances are all below 10 μH, the THD of both i_{p1} and i_{p2} remains low and exhibits minimal variation. It indicates that weak interchannel coupling in this range has a negligible impact on the current quality of both channels, ensuring stable and undistorted operation.

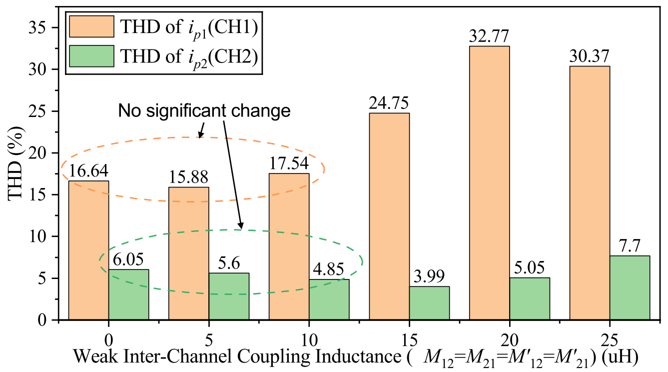

Fig. 3. Influence of weak interchannel coupling inductances on current THD in CH1 and CH2.

According to (5) and Fig. 3, when M_{12}, M'_{12}, M_{21}, M'_{21} $<<$ L_{p1}, L_{p2}, L_{s1}, L_{s2}, their influence on the currents becomes negligible. Consequently, the weak interchannel coupling inductances M_{12}, M_{21}, M'_{12}, and M'_{21} can be disregarded in the subsequent power transfer and ZVS analysis.

By applying the superposition theorem for different subharmonics and the KVL equation, while ignoring parasitic parameters, equivalent series resistance (ESR), and harmonics at frequencies other than the resonance frequency of this channel, the following equation is obtained:

$$\begin{cases} \dot{U}_{ab.1} = \left(j\omega L_{p1} + \frac{1}{j\omega C_{p1}}\right) \cdot \dot{I}_{p1} - j\omega M_1 \dot{I}_{s1} \\ \dot{U}_{ag.3} = \left(j3\omega L_{p2} + \frac{1}{j3\omega C_{p2}}\right) \cdot \dot{I}_{p2} - j3\omega M_2 \dot{I}_{s2} \\ 0 = \left(j\omega L_{s1} + \frac{1}{j\omega C_{s1}}\right) \cdot \dot{I}_{s1} + \dot{U}_{co} - j\omega M_1 \dot{I}_{p1} \\ 0 = \left(j3\omega L_{s2} + \frac{1}{j3\omega C_{s2}}\right) \cdot \dot{I}_{s2} + \dot{U}_{od} - j3\omega M_2 \dot{I}_{p2} \end{cases} \tag{6}$$

where $U_{ab.1}$ represents fundamental component of u_{ab}, and $U_{ag.3}$ represents the third harmonic component of u_{ag}. By (1) and (2), the root mean square (rms) port voltages are given by

$$\begin{aligned} &U_{ab.1} = 2\sqrt{2} V_{\text{bus}} \sin(\pi D) \Big/ \pi \\ &U_{ag.3} = \sqrt{2} V_{\text{bus}} \Big/ 3\pi; U_{co} = U_{od} = \sqrt{2} U_o \Big/ \pi. \end{aligned} \tag{7}$$

Similarly, the port voltages of secondary side are given by

$$\begin{cases} u_{co} = \sum_{n=1}^{\infty} \frac{2U_o \cdot \sin(0.5n\pi)}{\pi} \cdot \sin(\omega_1 t + \varphi_{co}) \\ u_{od} = \sum_{n=1}^{\infty} \frac{2U_o \cdot \sin(0.5n\pi)}{\pi} \cdot \sin(3\omega_1 t + \varphi_{od}) \end{cases} \tag{8}$$

where u_{co} and u_{od} represent the output port voltages of CH1 and CH2, respectively. As shown in Fig. 2, $\Delta\varphi_{s2}$ represents the phase shift angle between i_{s2} and u_{od}. When $\Delta\varphi_{s2} = 0$, H3 operates in synchronous rectification mode (SRM). Conversely, when $\Delta\varphi_{s2} \neq 0$, H3 operates in the third harmonic phase shift mode (3HPSM). Based on (6) and (7), when $\omega = \omega_1$, the rms current can be derived as follows:

$$\begin{cases} I_{s1} = \frac{2\sqrt{2}V_{\text{bus}}\sin(\pi D)}{\pi\omega_1 M_1}; I_{s2} = \frac{\sqrt{2}V_{\text{bus}}}{9\pi\omega_1 M_2} \\ I_{p1} = \frac{\sqrt{2}U_o}{\pi\omega_1 M_1}; I_{p2} = \frac{\sqrt{2}U_o}{3\pi\omega_1 M_2}. \end{cases} \tag{9}$$

Therefore, the power for each channel can be expressed as

$$P_{\text{CH1}} = U_{ab.1} \cdot I_{p1} = \frac{4V_{\text{bus}}U_o\sin(\pi D)}{\pi^2\omega_1 M_1}$$

$$P_{\text{CH2}} = U_{ag.3} \cdot I_{p2}\cos\left(\Delta\varphi_{s2}\right) = \frac{2V_{\text{bus}}U_o\cos(\Delta\varphi_{s2})}{9\pi^2\omega_1 M_2}. \tag{10}$$

Thus, the total output power of the two channels is as

$$P_{\text{Total}} = P_{\text{CH1}} + P_{\text{CH2}} = \frac{4V_{\text{bus}}U_o\sin(\pi D)}{\pi^2\omega_1 M_1} + \frac{2V_{\text{bus}}U_o\cos\Delta\varphi_{s2}}{9\pi^2\omega_1 M_2}. \tag{11}$$

When the output load is equivalent to a resistor, the output current can be expressed as

$$\begin{aligned} I_L &= \frac{1}{T_o}\int_0^{T_O/2}\sqrt{2}i_{s1}\sin(\omega_1 t)dt + \frac{3}{T_o}\int_0^{T_o/6} \\ &\quad\times\sqrt{2}i_{s2}\sin(3\omega_1 t + \Delta\varphi_{s2})dt \\ &= \frac{\sqrt{2}I_{s1}}{\pi} + \frac{\sqrt{2}I_{s2}\cos(\Delta\varphi_{s2})}{\pi}. \end{aligned} \tag{12}$$

The output voltage can be equivalently expressed as

$$U_o = \frac{4V_{\text{bus}}R_L\sin(\pi D)}{\pi^2\omega_1 M_1} + \frac{2V_{\text{bus}}R_L\cos(\Delta\varphi_{s2})}{9\pi^2\omega_1 M_2}. \tag{13}$$

B. Loss Analysis of Proposed F3HDC-WPT System

According to [31] and [32], the total loss P_{Loss} of the proposed F3HDC-WPT system can be expressed as

$$\begin{cases} P_{Loss} = P_{cu} + P_{S.cond} + P_{S.sw} + P_D + P_{Cap} \\ P_{cu} = I_{p1}^2 \cdot R_{p1} + I_{p2}^2 \cdot R_{p2} + I_{s1}^2 \cdot R_{s1} + I_{s2}^2 \cdot R_{s2} \\ P_{S.cond} = I_{p1}^2 \cdot R_S + \left(I_{p1}^2 + I_{p2}^2\right) \cdot R_S + I_{s2}^2 \cdot R_S \\ P_{S.sw} \approx P_{Sw.\text{off}} \approx 4 \cdot \frac{I_{\varepsilon.p}^2 t_{f1}^2 f_o}{24C_{oss}} + 2 \cdot \frac{I_{\varepsilon.s}^2 t_{f2}^2 3f_o}{24C_{oss}} \\ P_D \approx P_{D.cond} = V_F \cdot I_{s1.av} + R_D \cdot I_{s1}^2 \\ \quad = \frac{2\sqrt{2}V_F I_{s1}}{\pi} + R_D \cdot I_{s1}^2 \\ P_{Cap} = I_{p1}^2 \cdot R_{C.p1} + I_{p2}^2 \cdot R_{C.p2} + I_{s1}^2 \cdot R_{C.s1} + I_{s2}^2 \cdot R_{C.s2} \end{cases} \tag{14}$$

where P_{cu} denotes the copper loss of coils and wires, and $P_{S.cond}$ represents the conduction losses of all switches (S_1–S_4 and Q_1-Q_2). The switching losses of all switches are denoted as $P_{S.sw}$, where only turn-OFF losses are considered due to the realization of ZVS. The total diode losses are represented by P_D. Since the switching and turn-OFF losses of Schottky diodes are negligible, diode losses can be approximated by their conduction losses, denoted as $P_{D.cond}$. The equivalent resistance of the coupler coils is P_{Cap}. The equivalent resistances of the coupler coils and wires are denoted as R_{p1}, R_{p2}, R_{s1}, and R_{s2}. The conduction loss of a single MOSFET is represented by R_S. The initial current magnitudes at the beginning of the switching period are given by $I_{\varepsilon.p}$ and $I_{\varepsilon.s}$. The current fall times to zero for S_1–S_4 and Q_1-Q_2 are denoted as t_{f1} and t_{f2}, respectively. The MOSFET parasitic capacitance is represented as C_{oss}. The average diode current is denoted as $I_{s1.av}$, the forward voltage as V_F, and the diode conduction resistance as R_D. The conduction resistances of the resonant capacitors are given by $R_{C.p1}$, $R_{C.p2}$, $R_{C.s1}$, and $R_{C.s2}$.

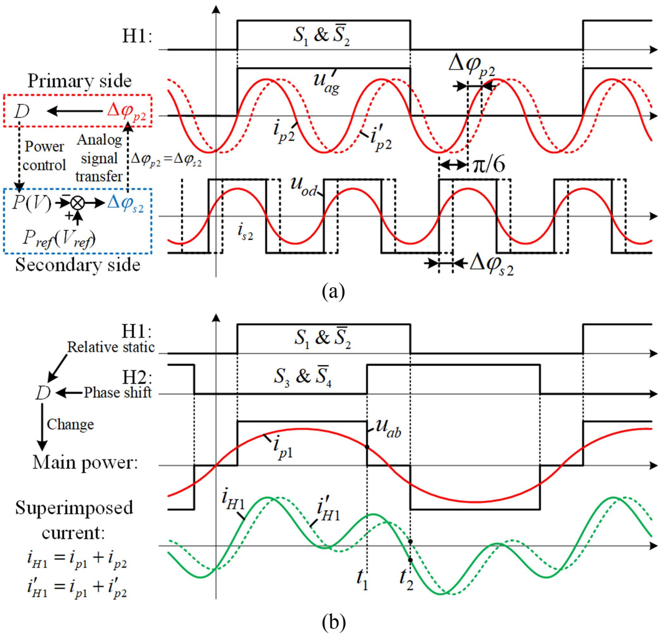

Fig. 4. Waveforms and control method of the proposed system in two mode. (a) Waveforms of CH2 in SRM and 3HPSM modes. (b) Waveforms of CH1 in SRM and 3HPSM modes.

The overall dc–dc conversion efficiency of the proposed system can be defined as

$$\eta_{\text{dc--dc}} = \frac{P_{\text{Total}}}{P_{\text{Total}} + P_{\text{Loss}}} = \frac{U_o \cdot I_L}{V_{\text{bus}} \cdot I_{\text{in}}}. \tag{15}$$

C. Current and Operation Waveform Analysis

By configuring the parameters to satisfy (3), the resonant current consists of the first and third harmonic current. Ignoring the weak coupling mutual inductance and the ESR of coils and other components, the waveforms in different mode are shown in Fig. 4.

When Q_1&Q_2 operate in SRM, the waveforms of CH2 are, as shown by the solid line in Fig. 4(a), and the power factor is equal to 1. In contrast, when Q_1&Q_2 operate in 3HPSM, the waveform of CH2 is depicted by the dashed line. Meanwhile, the phase between the u_{od} and the i_{s2} is $\Delta\varphi_{s2}$. According to (6), when $\omega = \omega_1$, the phase relationship between U_{od} and I_{p2} is expressed as follows:

$$\dot{U}_{od} = j3\omega M_2\dot{I}_{p2}. \tag{16}$$

Due to the characteristics of the S–S resonant circuit, the phase shift $\Delta\varphi_{p2}$ between u_{ag} and i_{p2} varies with $\Delta\varphi_{s2}$ and is equal to it. To enable power/voltage control without communication, the power/voltage error collected on the secondary side is converted

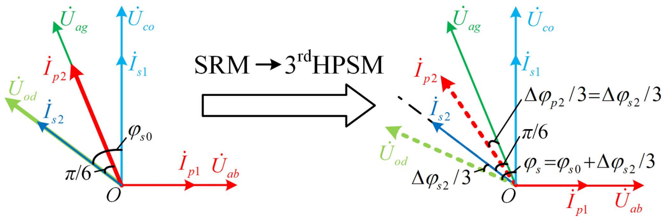

Fig. 5. Vectors for the proposed system from SRM to 3HPSM.

into $\Delta\varphi_{s2}$ controlled by H3. The analog value of $\Delta\varphi_{s2}$ is transmitted to the primary side as $\Delta\varphi_{p2} = \Delta\varphi_{s2}$. On the primary side, the detected $\Delta\varphi_{p2}$ is used to adjust D, which primarily determines the transmitted power according to (11).

As shown in Fig. 4(b), H1 is relatively static to ensure proper power and communication transmission of CH2. Meanwhile, H2 is applied for adjustment of the duty cycle D. As depicted in Fig. 5, the vector diagram adopts the fundamental frequency as the reference coordinate system. Consequently, the phase of the third harmonic channel CH2 in this coordinate system needs to be divided by 3. The phase of i_{s1} is chosen as the reference phase, since the current of CH1 remains relatively stable across various operating modes of CH2. In the SRM, the phase shift between the reference i_{s2} and u_{od} is detected and stored as φ_{s0}. When H3 operates in 3HPSM, its phase shift is determined by $\varphi_{s0} + \Delta\varphi_{s2}/3$.

In 3HPSM, when the resonance condition is not ideal or the mutual inductance varies, U_{od} in (6) is rewritten as follows:

$$\begin{aligned}\dot{U}_{od} &= j3\left(\omega_1 + \Delta\omega\right)\left(M_2 + \Delta M_2\right)\dot{I}_{p2}\\ &\quad - \left[j3\left(\omega_1 + \Delta\omega\right)\left(L_{s2} + \Delta L_{s2}\right)\right.\\ &\quad \left. + \frac{1}{j3\left(\omega_1 + \Delta\omega\right)\left(C_{s2} + \Delta C_{s2}\right)}\right]\cdot\dot{I}_{s2}\\ &\approx j3\left(\omega_1 M_2 + \Delta\lambda_1\right)\dot{I}_{p2} - \left(j3\omega_1 L_{s2} + \frac{1}{j3\omega_1 C_{s2}} + \Delta\lambda_2\right)\\ &\quad \cdot\dot{I}_{s2}\\ &= j3\left(\omega_1 M_2 + \Delta\lambda_1\right)\dot{I}_{p2} - \Delta\lambda_2\cdot\dot{I}_{s2} \end{aligned} \tag{17}$$

where $\Delta\omega$, ΔL_{s2}, and ΔC_{s2} represent the errors of different parameter. The $\Delta\lambda_1$ and $\Delta\lambda_2$ represent the equivalent error values. The phase of i_{p2} caused by parameters errors is as

$$\Delta\varphi_{p2} = \arctan\left(\frac{U_{od}\sin\Delta\varphi_{s2}}{U_{od}\cos\Delta\varphi_{s2} - \Delta\lambda_2}\right) \approx \Delta\varphi_{s2} + \Delta\zeta \tag{18}$$

where $\Delta\zeta$ is the phase deviation caused by parameters and other errors. In practical application, the PI controller can be introduced to eliminate this error.

However, as depicted in Fig. 4(b), when operating in SRM, the superimposed current i_{H1} cannot meet the wide range ZVS condition of the shared arm H1, regardless of the presence of the third harmonic current. However, with the inductive current i_{p2}, the superimposed current i'_{H1} has the potential for wide-range ZVS. The detailed ZVS analysis is as above.

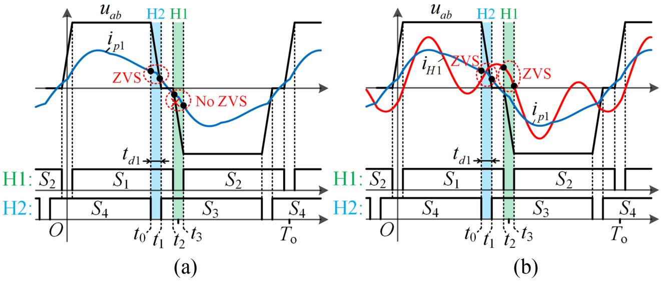

(a) (b)

Fig. 6. ZVS condition analysis of WPT system. (a) For the traditional system. (b) For the proposed F3HDC-WPT system.

D. ZVS Condition Analysis

The ZVS analysis is depicted in Fig. 6. The blue waveforms represent the primary-side current i_{p1} of CH1, and the red waveform represents the primary-side superimposed current i_{H1} of the proposed system.

1) ZVS Condition Analysis of Traditional System: The traditional single-channel wireless power transfer (SC-WPT) system includes only the CH1. Since the current waveform within a switching period is symmetrical, only one switching mode needs to be analyzed for each bridge arm. As depicted in Fig. 6(a), the current flowing through both H1 and H2 is i_{p1} as blue waves depicted. The ZVS condition of H-bridge on primary side is given by

$$i_{p1\_t1} \geq 0, \quad \int_{t_0}^{t_1} i_{p1}dt \geq 2C_{oss}V_{\text{bus}} \tag{19}$$

where t_0 and t_1 denote the start time and the end time of the switching dead zone, respectively. C_{oss} represents the output parasitic capacitance. The short time sinusoidal current can be approximately treated as linear change. Thus, the ZVS condition of H2 as (19) can be equivalently expressed as

$$i_{p1\_t1} \geq 0, \quad \frac{\left(i_{p1\_t0} + i_{p1\_t1}\right)}{2} \approx i_{p1\_s}(DT_o) \geq \frac{2C_{oss}V_{\text{bus}}}{t_{d1}}. \tag{20}$$

Similarly, the ZVS condition of H1 is given by

$$i_{p1\_t3} \geq 0, \quad \frac{i_{p1\_t2} + i_{p1\_t3}}{2} \approx i_{p1\_s}(0.5T_o) \geq \frac{2C_{oss}V_{\text{bus}}}{t_{d1}} \tag{21}$$

where $t_{d1} = t_1 - t_0 = t_3 - t_2$ represents the dead zone time for H1 and H2. For CH1, due to its bandpass characteristics, higher-order harmonics are not transmitted between the primary and secondary sides. Neglecting internal resistance, the higher-order harmonics current of i_{p1} can be approximately expressed as

$$i_{p1\_n} \approx \frac{4V_{\text{bus}}\sin(n\pi D)}{n\pi}\cdot\frac{\sin\left[n\omega_1 t + \pi(1-2nD)/2\right]}{jn\omega_1 L_{p1} + 1/jn\omega_1 C_{p1}}$$
$$(n = 3, 5, \cdots). \tag{22}$$

According to (22), the amplitude of the fifth, seventh, and higher order current components is relatively small. By ignoring the fifth and higher order harmonics, the i_{p1} can be expressed as

$$\begin{aligned} i_{p1\_s} &= i_{p1\_1st} + i_{p1\_3rd} \\ &= \frac{2U_o\cos(\omega_1 t - \pi D)}{\pi\omega_1 M_1} + \frac{V_{\text{bus}}\sin(3\pi D)\sin(3\omega_1 t - 3\pi D)}{2\pi\omega_1 L_{p1}}. \end{aligned} \tag{23}$$

Based on (23), the (20) and (21) can be expressed as

$$i_{p1\_s}(DT_o) = \frac{2U_o\cos(\pi D)}{\pi\omega_1 M_1} + \frac{V_{\text{bus}}\sin^2(3\pi D)}{2\pi\omega_1 L_{p1}} \geq \frac{2C_{oss}V_{\text{bus}}}{t_{d1}} \tag{24}$$

$$i_{p1\_s}(0.5T_o) = -\frac{2U_o\cos(\pi D)}{\pi\omega_1 M_1} + \frac{V_{\text{bus}}\sin^2(3\pi D)}{2\pi\omega_1 L_{p1}} \geq \frac{2C_{oss}V_{\text{bus}}}{t_{d1}}. \tag{25}$$

From (24), the ZVS condition for H2 can be achieved in the range of $D = 0 \sim 0.5$ through appropriate parameters design. However, as indicated by (25), achieving ZVS for H1 becomes impossible when D is relatively small, regardless of system parameters. Consequently, the traditional single-channel system operating at the fundamental frequency suffers from low efficiency when D is small.

As analyzed above, achieving ZVS for H1 across the full power range is challenging. The proposed system introduces CH2 to H1, enabling the harmonic current i_{p2} to flow through H1, thereby creating favorable conditions for ZVS.

2) ZVS Condition Analysis of the Proposed System: In the proposed F3HDC-WPT system, the current and ZVS conditions for H2 remain the same as in the traditional system. However, the current of H1 is modified, as represented by the red waveforms in Fig. 6(b). The ZVS condition for H1 is updated

$$\begin{cases} i_{\text{H1}\_t2} = i_{p1\_t2} + i_{p2\_t2} > 0 \\ (i_{\text{H1}\_t2} + i_{\text{H1}\_t3})/2 = i_{\text{H1}}(0.5T_o) \geq 2C_{oss}V_{\text{bus}}/t_{d1} \end{cases}. \tag{26}$$

For CH2, due to the bandpass characteristics of the third filter, which is composed of L_{p2}, C_{p2}, L_{s2}, and C_{s2}, the first, fifth, and higher order harmonics are not transmitted between the primary and secondary sides. As a result, all harmonic components of i_{p2}, except for the third harmonic, can be approximated as follows:

$$i_{p2\_n} \approx \frac{2V_{\text{bus}}}{n\pi} \cdot \frac{\sin(n\omega_1 t)}{jn\omega_1 L_{p2} + 1/jn\omega_1 C_{p2}}\ (n = 1, 5, 7, \cdots). \tag{27}$$

Ignoring the fifth and higher order harmonic components, the current i_{H1} of the H1 can be expressed as

$$\begin{aligned} i_{\text{H1}\_s} &= i_{p1\_1st} + i_{p2\_3rd} + i_{p1\_3rd} + i_{p2\_1st} \\ &= \frac{2U_o\cos(\omega_1 t - \pi D)}{\pi\omega_1 M_1} + \frac{2U_o\sin(3\omega_1 t - \Delta\varphi_{s2})}{3\pi\omega_1 M_2} \\ &\quad + \frac{V_{\text{bus}}\sin(3\pi D)\sin(3\omega_1 t - 3\pi D)}{2\pi\omega_1 L_{p1}} + \frac{V_{\text{bus}}\cos(\omega_1 t)}{4\pi\omega_1 L_{p2}}. \end{aligned} \tag{28}$$

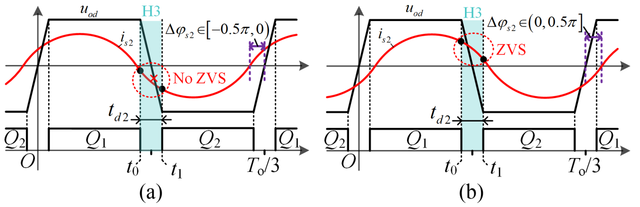

Fig. 7. ZVS condition analysis for secondary side of the proposed system. (a) Phase of current advanced to voltage. (b) Phase of current delayed to voltage.

Combining (26) and (28), the ZVS condition of H1 is as

$$\begin{aligned} i_{\text{H1}\_s}\left(\frac{T_o}{2}\right) &= \frac{-2U_o\cos(\pi D)}{\pi\omega_1 M_1} + \frac{2U_o\sin(\Delta\varphi_{s2})}{3\pi\omega_1 M_2} \\ &\quad + \frac{V_{\text{bus}}\sin^2(3\pi D)}{2\pi\omega_1 L_{p1}} - \frac{V_{\text{bus}}}{4\pi\omega_1 L_{p2}} \geq \frac{2C_{oss}V_{\text{bus}}}{t_{d1}}. \end{aligned} \tag{29}$$

According to (29), the most challenging condition for ZVS occurs when $D \approx 0$. However, ZVS can still be achieved by adjusting $\Delta\varphi_{s2}$, which is controlled by H3 on the secondary side.

3) Secondary Side's ZVS Condition of the Proposed System: On the secondary side, the potential hard switching occurs only on H3. As shown in Fig. 7, the ZVS condition for H3 is

$$i_{p1\_t1} \geq 0, \quad (i_{s2\_t0} + i_{s2\_t1})/2 \approx i_{s2}(T_o/6) \geq C_{oss}U_o/t_{d2}. \tag{30}$$

Comparing Fig. 7(a) and (b), it is evident that H3 achieves ZVS only when $\Delta\varphi_{s2}$ is within the interval $(0, 0.5\pi]$. Only a small portion of other order harmonics components is transmitted to the secondary side. Therefore, the i_{s2} can be approximated as

$$i_{s2} = 2V_{\text{bus}}\sin(3\omega_1 t - \Delta\varphi_{s2})/(9\pi\omega_1 M_2). \tag{31}$$

As shown in Fig. 7(b), ZVS condition for H3 is expressed as

$$i_{s2}(T_o/6) = 2V_{\text{bus}}\sin(\Delta\varphi_{s2})/9\pi\omega_1 M_2 \geq C_{oss}U_o/t_{d2}. \tag{32}$$

E. Parameters Design

Typically, the voltage rating of the resonant capacitors in the WPT system greatly constrains the parameters design of the system. Allowing a 20% margin for the voltage rating of the resonant capacitors, the voltage rating constraints for the four resonant capacitors in the system are as follows:

$$\begin{cases} U_{Cp1} = I_{p1} \cdot \omega_1 L_{p1} = \sqrt{2}U_o L_{p1}/\pi M_1 \leq 0.8U_{\text{lim}} \\ U_{Cp2} = I_{p2} \cdot 3\omega_1 L_{p2} = \sqrt{2}U_o L_{p2}/\pi M_2 \leq 0.8U_{\text{lim}} \\ U_{Cs1} = I_{s1} \cdot \omega_1 L_{s1} = 2\sqrt{2}V_{\text{bus}} L_{s1}/\pi M_1 \leq 0.8U_{\text{lim}} \\ U_{Cs2} = I_{s2} \cdot 3\omega_1 L_{s2} = \sqrt{2}V_{\text{bus}} L_{s2}/3\pi M_2 \leq 0.8U_{\text{lim}} \\ L_{p1} = L_{s1}, L_{p2} = L_{s2}. \end{cases} \tag{33}$$

For improved filtering performance, L_{p1}, L_{p2}, L_{s1}, L_{s2} should be designed to relatively large, whereas M_1 and M_2 should be minimized to enhance transfer power.

TABLE I
SYSTEM CONFIGURATION PARAMETERS

Parameters	V_{bus}	U_o	f_o	C_{oss}	R_{p1}, R_{s1}
Value	400 V	150 V–300 V	100 kHz	73.6 pF	0.6 Ω
Parameters	t_{d1}/t_{d2}	L_{p1}/L_{p2}	U_{lim}	P_{out}	R_{p2}, R_{s2}
Value	200/66.7 ns	130/80 μH	2 kV	1.7 kW	0.4 Ω
Parameters	R_S/R_D	$R_{C.p1}/R_{c.p2}/R_{C.s1}/R_{C.s2}$		V_F	t_{f1}/t_{f2}
Value	80 mΩ/54 mΩ	50 mΩ		0.43 V	18 ns

According to (29), when $\Delta\varphi_{s2} = 0.5\pi$, the current in CH2 maximizes the ZVS condition for H1, indicating that the CH2 operates in a purely inductive reactive mode.

By combining (24), (29), and (32), the ZVS boundary conditions ($\Delta\varphi_{s2} = \pi/2$) for all switches can be organized as

$$\begin{cases} \frac{2U_o\cos(\pi D)}{\pi\omega_1 M_1} + \frac{V_{\text{bus}}\sin^2(3\pi D)}{2\pi\omega_1 L_{p1}} \geq \frac{2C_{oss}V_{\text{bus}}}{t_{d1}} \\ \frac{2U_o}{3\pi\omega_1 M_2} - \frac{2U_o\cos(\pi D)}{\pi\omega_1 M_1} + \frac{V_{\text{bus}}\sin^2(3\pi D)}{2\pi\omega_1 L_{p1}} - \frac{V_{\text{bus}}}{4\pi\omega_1 L_{p2}} \geq \frac{2C_{oss}V_{\text{bus}}}{t_{d1}} \\ \frac{2V_{\text{bus}}}{9\pi\omega_1 M_2} \geq \frac{C_{oss}U_o}{t_{d2}}. \end{cases} \tag{34}$$

Considering the total power loss of the F3HDC-WPT system, as expressed in (14)

$$\begin{aligned} P_{\text{Loss}} \approx\ & I_{p1}^2 \cdot (R_{p1} + 2R_S + R_{C.p1}) + I_{p2}^2 \\ & \cdot (R_{p2} + R_S + R_{C.p2}) \\ & + I_{s1}^2 \cdot (R_{s1} + R_D + R_{C.s1}) + \frac{2\sqrt{2}V_F I_{s1}}{\pi} \\ & + I_{s2}^2 \cdot (R_{s2} + R_S + R_{C.s2}) + \frac{I_{\varepsilon.p}^2 t_{f1}^2 f_o}{6C_{oss}} + \frac{I_{\varepsilon.s}^2 t_{f2}^2 f_o}{4C_{oss}}. \end{aligned} \tag{35}$$

The system fixed parameters are shown in Table I. The dead zone time is set to 2% of the switching period, with $t_{d1} = 200$ ns, $t_{d2} = 66.7$ ns. The voltage limitation of resonant capacitors is 2 kV. To simplify the calculation, the switching losses in (35) can be neglected, as they are minimal according to the parameters listed in Table I.

In addition, for the rated power of 1.7 kW, the system should be capable of delivering more than 1.7 kW when $D = 0.5$ and $\Delta\varphi_{s2} = 0$. Under this condition, (8) can be rewritten as

$$\frac{4V_{\text{bus}}U_o}{\pi^2\omega_1 M_1} + \frac{2V_{\text{bus}}U_o}{9\pi^2\omega_1 M_2} \geq 1700. \tag{36}$$

By combining (23), (35), and (36) and the parameters listed in Table I, the expression of mutual inductance can be organized as follows:

$$\begin{cases} f_1(M_1, M_2) = \frac{50.66\times10^{-6}}{M_2} - \frac{122.96\times10^{-6}}{M_1} \geq 0.2227 \\ f_2(M_1, M_2) = \frac{77.40\times10^{-6}}{M_1} + \frac{4.30\times10^{-6}}{M_2} \geq 1.7 \\ \min\left(P_{\text{Loss}} = \frac{2.674\times10^{-7}}{M_1^2} + \frac{2.219\times10^{-4}}{M_1} + \frac{3.461\times10^{-9}}{M_2^2}\right). \end{cases} \tag{37}$$

Considering the overall design constraints, including loss, the design point is chosen within the ZVS region and power range defined by (37). The feasible region satisfying both f_1 and f_2 is shown in red in Fig. 8, along with the loss contours of P_{loss}. The calculated optimal point, minimizing losses while meeting both constraints, is $M_1 = 52.6\,\mu$H, $M_2 = 19.7\,\mu$H.

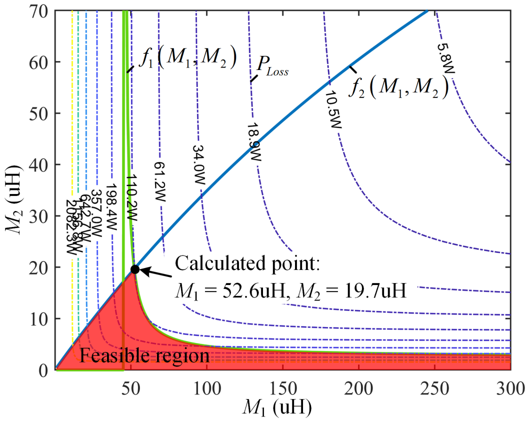

Fig. 8. Parameters design and available area for considering the full ZVS area of the proposed system.

In the interval $(0, 0.5\pi]$, as $\Delta\varphi_{s2}$ increases, the reactive power in CH2 also increases, which is detrimental to the transmission efficiency of the system. Therefore, based on the design point, the dynamic relationship between $\Delta\varphi_{s2}$ and D can be calculated based on (29) as follows:

$$\sin(\Delta\varphi_{s2}) \geq \frac{3M_2\cos(\pi D)}{M_1} + \frac{3M_2 V_{\text{bus}}}{2U_o} \times \left(\frac{2\pi\omega_1 C_{oss}}{t_{d1}} + \frac{1}{4L_{p2}} - \frac{\sin^2(3\pi D)}{2L_{p1}}\right). \tag{38}$$

This allows the system to dynamically adjust $\Delta\varphi_{s2}$ to ensure ZVS for all switches, when different power is transmitted by various values of D.

When coil misalignment occurs, both channels (CH1 and CH2) experience simultaneous spatial displacement. As a result, the mutual inductances M_1 and M_2 decrease in a similar trend. In this analysis, the ratio M_2/M_1 is approximated as a constant, which is a reasonable assumption based on the coil arrangement shown in Fig. 12 and the simulation results presented in Fig. 13.

Accordingly, (38) becomes a monotonically increasing function with respect to M_2. Therefore, as long as $\Delta\varphi_{s2}$ satisfies the requirement under the maximum M_2 condition (i.e., with ideal alignment), ZVS can be achieved under misaligned scenarios. The relationship between $\Delta\varphi_{s2}$ and D is expressed as follows:

$$\Delta\varphi_{s2} = \begin{cases} 0.5\pi, \quad D \leq 0.2 \\ \arcsin\left(1.12\cos(\pi D) - 0.15\sin^2(3\pi D) + 0.18\right), \\ \quad D > 0.2 \end{cases}. \tag{39}$$

Based on the parameters in Table I and the design point in Fig. 8, the relationship among D, $\Delta\varphi_{s2}$ and output power is depicted in Fig. 9(a). According to (39), the operation curve, minimizing reactive power in CH2 while ensuring ZVS for all switches, is plotted.

In order to evaluate the influence of CH2 on the overall efficiency, the coil losses of both channels are derived using

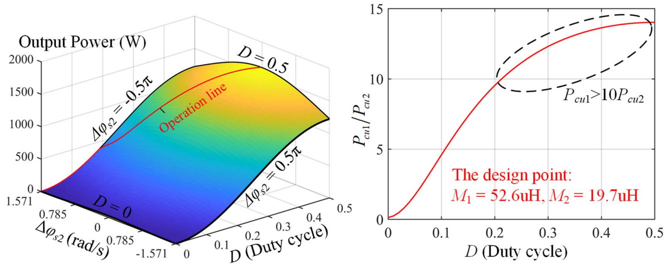

(a) (b)

Fig. 9. (a) Output power versus D and $\Delta\varphi_{s2}$. (b) Power ratio between CH1 and CH2 under varying D, with design point indicated.

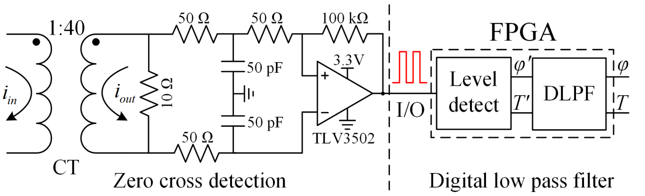

Fig. 10. ZCD-DLPF circuit and FPGA calculation principle.

(9) and (14) as follows:

$$\begin{cases} P_{cu1} = I_{p1}^2 \cdot R_{p1} + I_{s1}^2 \cdot R_{s1} = \frac{2U_o^2 R_{p1} + 8V_{\text{bus}}^2 \sin^2(\pi D) R_{s1}}{\pi^2 \omega_1^2 M_1^2} \\ P_{cu2} = I_{p2}^2 \cdot R_{p2} + I_{s2}^2 \cdot R_{s2} = \frac{18U_o^2 R_{p2} + 2V_{\text{bus}}^2 R_{s2}}{81\pi^2 \omega_1^2 M_2^2}. \end{cases} \tag{40}$$

Based on the design point shown in Fig. 8 and the loss expressions in (40), the ratio of copper loss between CH1 and CH2 is illustrated in Fig. 9(b). It can be observed that across most of the duty cycle range, P_{cu1} is significantly higher than P_{cu2}, especially when $D > 0.2$, where the ratio exceeds 10. This indicates that the contribution of CH2 to total copper loss is negligible, and thus, its impact on overall coil-to-coil efficiency is minimal.

F. Synchronization Control Strategy of F3HDC-WPT

To achieve communication-free control and wide-range ZVS for all switches in the proposed F3HDC-WPT system, an effective dynamic control strategy is essential. Power regulation is implemented by adjusting D, which requires detecting phase differences between voltages and currents or between different current signals in 3HPSM, as illustrated in Fig. 4(a). The phase of u_{ag} and u_{od} can be equivalently represented by the phase of PWM signal. For resonant current sampling, high-frequency digital sampling (HFDS) is costly, implementation-intensive, and susceptible to interference. To overcome these limitations, a zero-crossing detector (ZCD) is employed for current phase detection, as illustrated in Fig. 10. The ZCD circuit, composed of a current transformer and a comparator, converts current zero-crossing points into digital rising edges, allowing the FPGA to directly measure the signal's phase and period. To further enhance measurement reliability, a digital low-pass filter (DLPF) is implemented in the FPGA.

Since there are no communication devices in the system, a synchronization control method (SCM) is required for both the primary and secondary sides. The proposed SCM included two stages, as shown in Fig. 11(a)–(d).

In stage 1, CH2 operates in SRM, with an initial duty cycle of D_0. The initial D_0 is essential for system startup and synchronization. It ensures that both the primary and secondary sides generate current simultaneously, enabling reliable phase detection and stable initialization. If D_0 is too small, the current waveform becomes distorted, making zero-crossing detection unreliable. If too large, the system's adjustment range is limited, which may affect stability. Therefore, D_0 is set to 0.3 to balance waveform quality and control flexibility. Current phases are detected using the ZCD-DLPF circuit, with detection points shown in Fig. 11(e). Based on D_0 and the clock of FPGA A, the controller generates the switching signals S_1–S_4, as shown in Fig. 11(a), driving the FB to produce the port voltages u_{ab}, while H1 produces u_{ag}.

The FPGA monitors the period variation of i_{p2}, calculating $\Delta T_{ip2} = T_{ip2}(t+1) - T_{ip2}(t)$ of i_{p2}, and checks if it remains within 5% of resonant period $T_o/3$ for 2048 consecutive cycles. If this is yes, the initialization of the primary side completes.

In Stage 1 on the secondary side, the D_1&D_2 and H3 operate in diodes rectification mode (DRM). The current periods of i_{s1} and i_{s2} are sampled by ZCD-DLPF 2&3, as shown in Fig. 11(b). Similar to the primary side, the FPGA calculates ΔT_{is1} and ΔT_{is2} to verify the stability of operation in DRM.

Under normal DRM operation, the currents on both the primary and secondary sides naturally hold the same fixed period. Therefore, even without communication, once each side independently detects that the current period has stabilized, it can individually complete Stage 1. Since the current periods are inherently synchronized, both sides will finish Stage 1 nearly at the same time, ensuring synchronized transition to Stage 2.

In addition, as reference of φ_{s1}, the relative phase φ_{s2_s1} is as

$$\varphi_{s2\_s1} = \varphi_{s2} - \varphi_{s1}. \tag{41}$$

When Stage 1 done, the φ_{s2_s1} is stored in memory as $\varphi_{s2\_s1\_0}$.

In stage 2, on the secondary side, based on the stored $\varphi_{s2\_s1\_0}$ from Stage 1 and the real-time sampled φ_{s1}, the φ_{s2} is calculated by (41). As shown in Fig. 11(d), a PI controller calculates $\Delta\varphi_{s2}$ to eliminate the error between V_{ref} and U_o. Meanwhile, it also compensates for phase deviations $\Delta\zeta$ caused by non-ideal resonance or mutual inductance variations, as described in (18). Since $\Delta\zeta$ indirectly affects the output voltage, the voltage-error-based PI control inherently compensates for this deviation, without the need to explicitly measure or estimate $\Delta\zeta$, thereby ensuring accurate and robust control of the system. The PWM signals for H3 are then modulated based on both φ_{s2} and $\Delta\varphi_{s2}$. Based on the characteristics of S–S circuit shown in Fig. 5 and discussed in Chapter *B*, the phase $\Delta\varphi_{s2}$ is inherently transferred to the primary side as $\Delta\varphi_{p2} = \Delta\varphi_{s2} + \Delta\zeta$ without an additional device.

On the primary side, $\Delta\varphi_{p2}$ is obtained by comparing the phase of u_{ag} and i_{p2}, as shown in Fig. 11(c). A PI controller

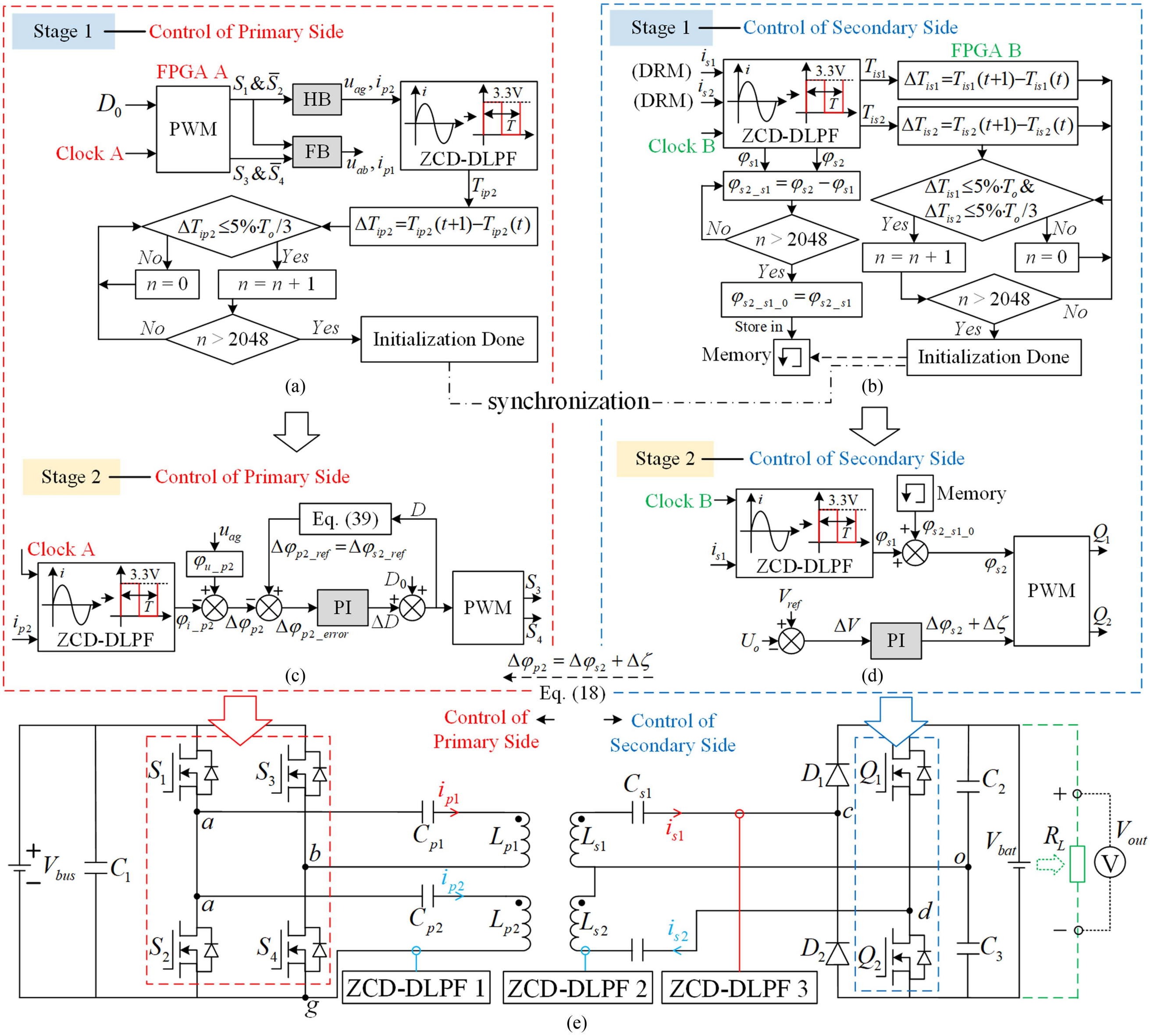

Fig. 11. Proposed 3HPSM of F3HDC-WPT system without communication. (a) Primary control in Stage 1. (b) Primary side control in Stage 2. (c) Secondary control in Stage 1. (d) Secondary control in Stage 2. (e) Sample point and sensors.

calculates D, based on the error between $\Delta\varphi_{p2\_ref}$ and $\Delta\varphi_{p2}$. The reference phase shift $\Delta\varphi_{p2\_ref}$ is calculated based on the desired ZVS condition using (39), which takes the real-time duty cycle D as input. Since $\Delta\varphi_{p2} \approx \Delta\varphi_{s2}$, the system sets $\Delta\varphi_{p2\_ref} = \Delta\varphi_{s2\_ref}$ on the primary side. The primary-side PI controller then adjusts D to drive the measured $\Delta\varphi_{p2}$ toward $\Delta\varphi_{p2\_ref}$. As a result, the secondary-side phase shift $\Delta\varphi_{s2}$ also follows $\Delta\varphi_{s2\_ref}$, closing the loop without requiring explicit communication. The resulting D is used to generate PWM signals S_3 and S_4 for power or voltage regulation.

G. Decoupling Principle

Fig. 12 illustrates the F3HDC-WPT system, which employs separate coils for CH1 and CH2 to enable efficient power transfer without the need for communication. In Fig. 12(a), the coupler configuration and dimensions are shown, where the orange and blue layers correspond to the coils for CH1 and CH2, respectively. CH1 adopts a pair of “D-D” type coils structure to transfer the fundamental power, while CH2 adopts a pair of “8-type” coils structure, as mentioned in [33], to transfer harmonic power and realize communication-free power control. Fig. 12(b) presents a three-dimensional (3-D) view of the transmitter and receiver, both CH1 and CH2 coils are designed with identical dimensions and are stacked vertically in a layered configuration to form a compact and symmetrical coupler structure. Fig. 12(c) illustrates the current paths of each coil. It can be observed that coils L_{p2} and L_{s2} in CH2, as well as coils L_{p1} and L_{s1} in CH1, achieve effective magnetic coupling. Meanwhile, due to the flux cancellation inherent in the “8-type” coils design of

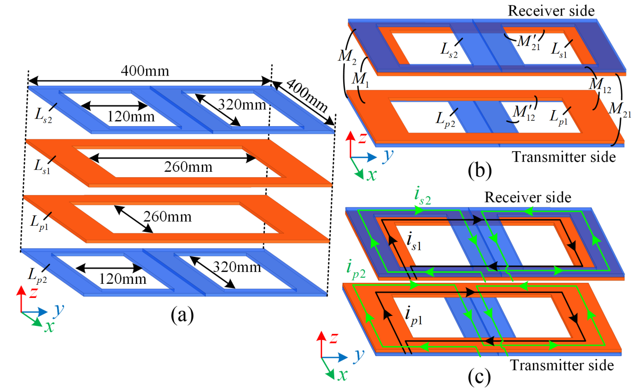

Fig. 12. Coupler system of proposed F3HDC-WPT. (a) Coupler arrangement and dimensions. (b) Three-dimensional view. (c) Decoupling analysis.

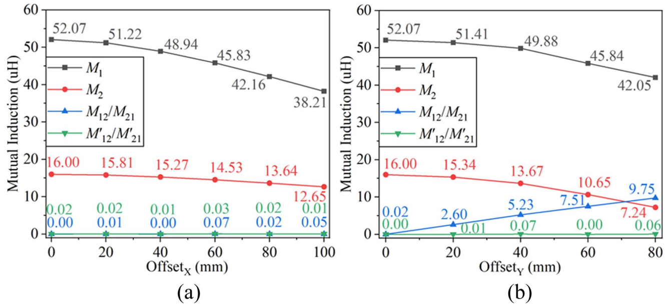

Fig. 13. Variations of mutual inductances under different offset conditions. (a) Offset along the X-axis. (b) Offset along the Y-axis.

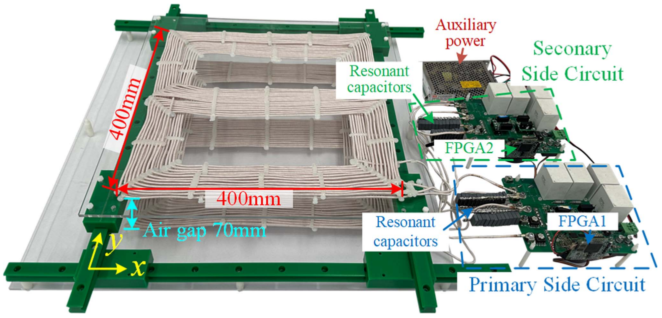

Fig. 14. Experimental platform.

TABLE II
SYSTEM CONFIGURATION PARAMETERS

Parameters	***Value***	***Parameters***	***Value***
V_{bus}	400V	f_o	100kHz
L_{p1}/L_{s1}(uH)	128.27/126.95	C_{p1}/C_{s1}(nF)	17.42/18.34
L_{p2}/L_{p2}(uH)	79.27/80.20	C_{p2} C_{s2}(nF)	4.08/4.21
M_1(uH)	54.66	M_{12}/M_{21}(uH)	0.34/1.34
M_2(uH)	21.23	M'_{12}/M'_{21}(uH)	0.68/3.53
R_{p1}/R_{s1}(Ω)	0.55/0.58	$R_{C.p1}/R_{C.p2}$(mΩ)	57/59
R_{p2}/R_{s2}(Ω)	0.43/0.39	$R_{C.s1}/R_{C.s2}$(mΩ)	52/61
Diodes(D_1, D_2)	S30T200C	MOSFETs(S_1–S_4, Q_1, Q_2)	P3M12080K3

CH2, the interaction between the harmonic coils $(L_{p2},\ L_{s2})$ and the fundamental coils $(L_{p1},\ L_{s1})$ is significantly suppressed, ensuring both magnetic and electrical isolation between the two channels.

Fig. 13 shows the simulated mutual inductance variations based on the coils structure shown in Fig. 12, obtained using Maxwell 3-D simulation. It illustrates the effect of misalignment along the X-axis (a) and Y-axis (b) on the mutual inductance values. As the offset along the X-axis and the Y-axis increases, the strongly coupled mutual inductances (M_1 and M_2) gradually decrease. Along the X-axis, the weakly coupled inductances $(M_{12},\ M_{21},\ M'_{12},$ and $M'_{21})$ remain near zero, indicating minimal magnetic interaction. In contrast, Y-axis misalignment leads to a gradual increase in weak mutual inductances. For instance, even at an 80 mm Y-axis offset, the maximum M_{12}/M_{21} reaches only 9.75 μH, which is still much smaller than L_{p1} and L_{s1}. According to the analysis of (5) and Fig. 3, the impact of these weakly coupled mutual inductances on power transfer can be ignored in system-level analysis.

III. EXPERIMENTAL VERIFICATION

A 1.7 kW experimental platform for the F3HDC-WPT system is established, as shown in Fig. 14. The coupler has a planar structure with a size of 400 mm × 400 mm, and the air gap between the primary and secondary sides is set to 70 mm. On both the primary and secondary sides, CH1 and CH2 coils are stacked together to form a compact and layered coupler structure. Both the primary and secondary sides are equipped with isolated FPGA control boards (FPGA1 and FPGA2), and auxiliary power is supplied to the control circuits. Resonant capacitors are connected on both sides to form the resonant network.

As shown in Table II, the system parameters are configured accordingly. The mutual inductance parameters are measured under the condition that the coupler is aligned without any XY offset.

A. *Experimental Results Without Misalignment*

For the steady-state experiment, the system is tested under a dc bus voltage of $V_{\text{bus}} = 400\,\text{V}$ with a resistive load of $R_L = 50\,\Omega$. The system operates stably under the 3HPSM, and the steady-state waveforms for different duty cycle D are presented in Fig. 15, where u_{S1_gs} is the gate drive voltage of switch S_1.

As illustrated in Fig. 15(a), when $D = 0.4$, both the superimposed current i_{H1} and the fundamental channel current i_{p1} satisfy the ZVS conditions for the corresponding bridge arms, ensuring soft-switching operation. When the duty cycles are reduced to $D = 0.3$ and $D = 0.2$, as shown in Fig. 15(b) and (c), ZVS is still maintained for both channels. However, a noticeable sine-wave distortion appears in i_{p1} and i_{p2}, indicating that lower duty cycles may introduce harmonic distortion in the current waveform, which is unfavorable for stable control. In practical testing, it was found that the system can maintain closed-loop operation down to a minimum duty cycle of $D = 0.15$ under ideal alignment. Below this threshold, the current waveform distortion becomes severe, and the system fails to sustain stable control.

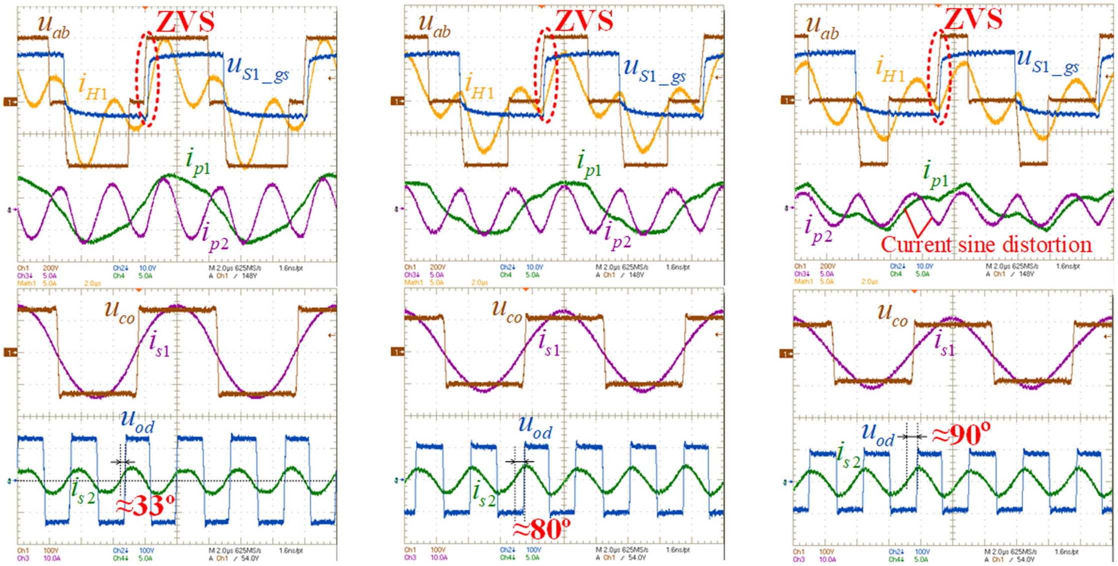

(a) (b) (c)

Fig. 15. Port voltages and currents waveforms on the primary and secondary sides for different D of u_{ab}. (a) $D = 0.4$. (b) $D = 0.3$. (c) $D = 0.2$.

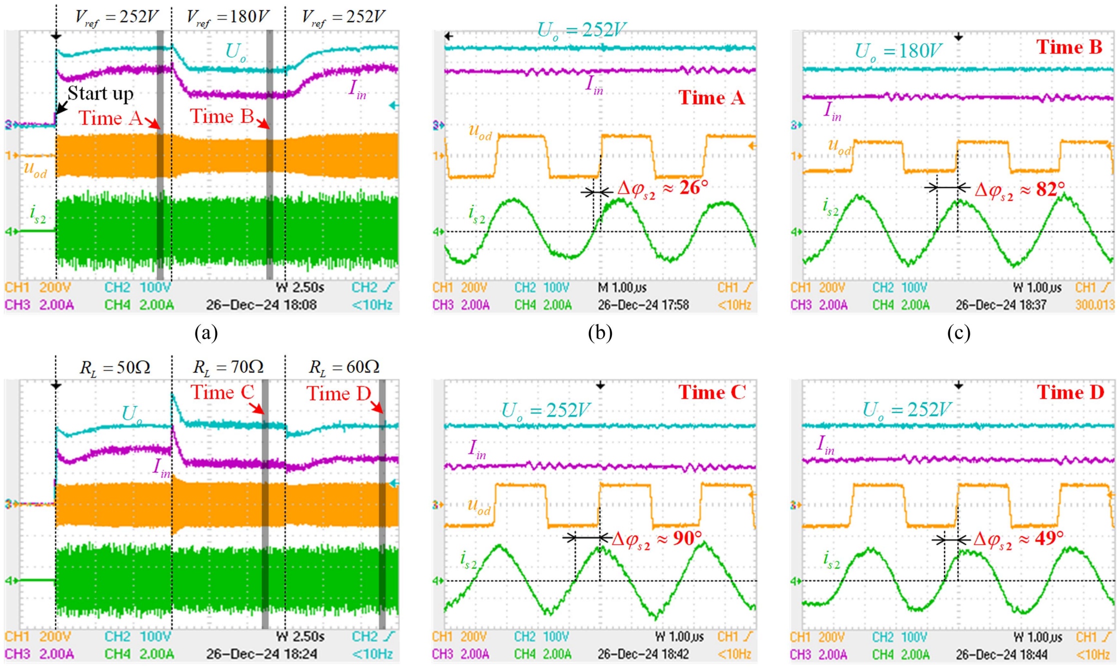

(a) (b) (c)

(d) (e) (f)

Fig. 16. Dynamic response of voltage and current waveforms. (a) Under different output voltages. (b) Detail waveforms at time A. (c) Detail waveforms at time B. (d) Under varying loads. (e) Detail waveforms at time C. (f) Detail waveforms at time D.

In addition, the current phase shift $\Delta\varphi_{s2}$ gradually increases as the duty cycle decreases. This shift is clearly visible in the bottom waveforms of Fig. 15, where the phase $\Delta\varphi_{s2}$ grows from approximately 33° at $D = 0.4$ to nearly 90° at $D = 0.2$, reflecting the dynamic behavior of the harmonic channel under different modulation depths.

Fig. 16 shows the system's dynamic response under varying reference voltages and load conditions, operating in closed-loop without communication. In Fig. 16(a), V_{ref} is adjusted between 252 V and 180 V, with a fixed resistive load $R_L = 50\ \Omega$. Fig. 16(b) and (c) presents detailed waveforms at Time A and Time B in Fig. 16(a), respectively. During this transition, the duty cycle automatically decreases with the drop in V_{ref}, and the system automatically increases $\Delta\varphi_{s2}$ of the CH2 from approximately 26° to 82°, to maintain ZVS under the reduced duty cycle D.

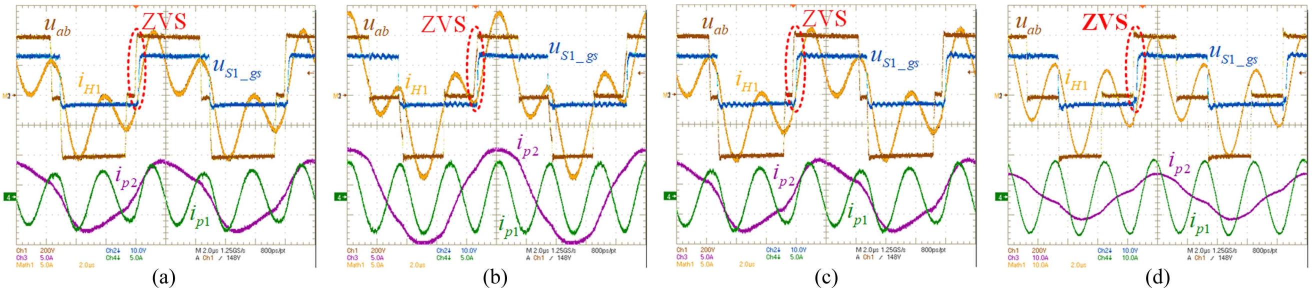

Fig. 17. Port voltage, resonant current, and ZVS waveforms on both primary and secondary sides for different duty cycles of u_{ab}. (a) X-axis offset = 20 mm. (b) Y-axis offset = 20 mm. (c) X-axis offset = 100 mm. (d) Y-axis offset = 80 mm.

In Fig. 16(d), R_L varies from 50 Ω to 70 Ω and 60 Ω, while V_{ref} is held constant at 252 V. The corresponding detailed waveforms at Time C and Time D are shown in Fig. 16(e) and (f). Similar to the voltage transition case, the system adaptively modulates $\Delta\varphi_{s2}$, increasing it up to 90° during light load and reducing it as the load increases again, ensuring ZVS operation.

These results confirm that the system can maintain wide-range ZVS conditions while achieving dynamic power control through the proposed 3HPSM.

B. Experimental Results Under XY-Axis Misalignment

Fig. 17 presents the steady-state waveforms of the system under four misalignment conditions: a) 20 mm offset along the X-axis, b) 100 mm offset along the X-axis, c) 20 mm offset along the Y-axis, and b) 80 mm offset along the Y-axis. These experiments were conducted under closed-loop control with a reference voltage $V_{ref} = 252\,\text{V}$. As a result, the duty cycle of the output voltage u_{ab} varies depending on the offset direction to regulate the output voltage accordingly. In both cases, ZVS is consistently maintained, as highlighted in the waveforms.

Fig. 18 shows the dynamic waveform response of the system under closed-loop operation with a reference voltage $V_{ref} = 252\,\text{V}$, when subject to misalignment along both the X-axis and Y-axis. Throughout the entire process, no wireless communication is used between the primary and secondary sides, demonstrating the stability of the proposed 3HPSM against significant variations in mutual inductance caused by positional deviations. The system maintains stable output voltage regulation by automatically adjusting the duty cycle D and the phase shift $\Delta\varphi_{s2}$ of CH2, as enabled by the proposed 3HPSM method.

The recommended misalignment distances are 100 mm along the X-axis and 80 mm along the Y-axis, corresponding to 25% and 20% of the 400 mm coil size, respectively. During the movement process, the system automatically reduces the duty cycle of u_{ab} to maintain a constant output voltage. To ensure ZVS under these conditions, the system automatically increases $\Delta\varphi_{s2}$ from approximately 21° to 90° for the X-axis case, and to 82° for the Y-axis case. Despite these significant adjustments, the output voltage remains well regulated, with peak deviations of 30 V and 36 V, respectively.

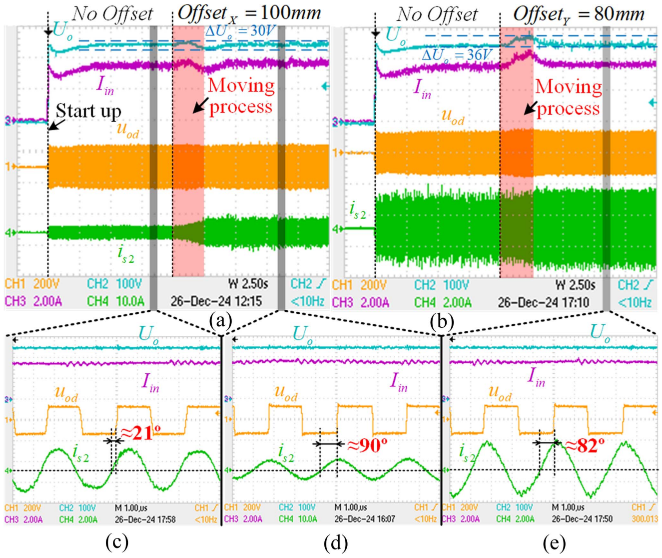

Fig. 18. Dynamic response of voltage and current waveforms under misalignment. (a) X-axis offset from 0 mm to 100 mm. (b) Y-axis offset from 0 mm to 80 mm. (c) Detail waveforms of no offset. (d) Detail waveforms of $Offset_X = 100\,\text{mm}$. (e) Detail waveforms of $Offset_Y = 80\,\text{mm}$.

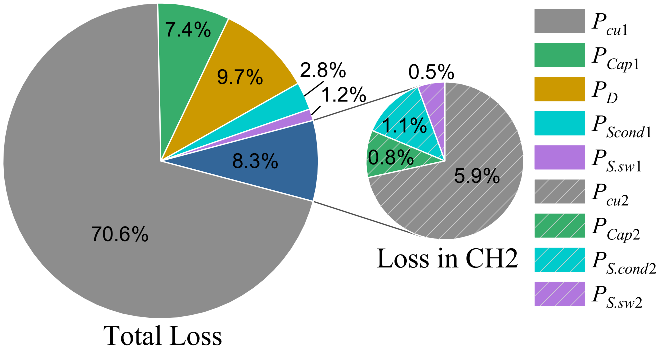

Fig. 19. Power loss distribution when P = 1680 W.

C. Power Loss and Efficiency Analysis

Fig. 19 illustrates the loss distribution of the system at the rated output power of 1680 W. As shown in the left pie chart, the primary contributor to the total system loss is the copper loss P_{cu1} in CH1, accounting for 70.6% of the total loss. While the

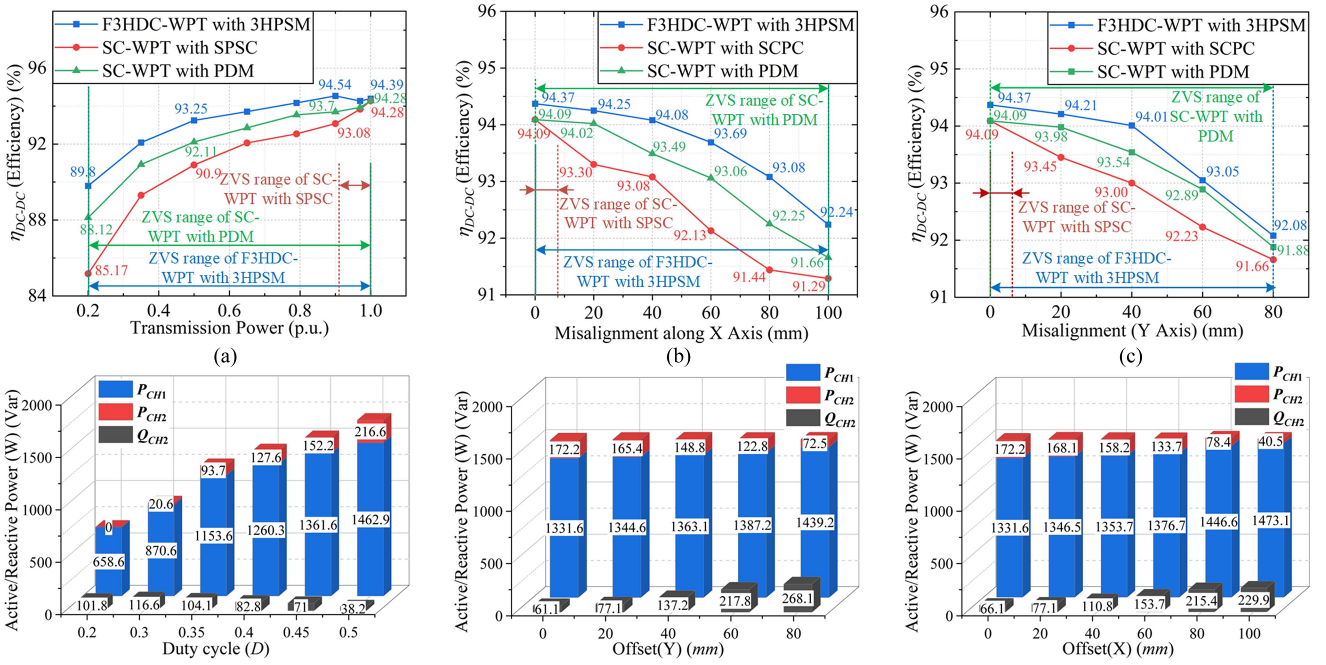

(a) (b) (c)

(d) (e) (f)

Fig. 20. Performance analysis of F3HDC-WPT and SC-WPT systems under different operating conditions. (a) ZVS range and efficiency with different transmission power. (b) ZVS range and efficiency with different $Offset_X$. (c) ZVS range and efficiency with different $Offset_Y$. (d) Power distribution with different D. (e) Power distribution with different $Offset_X$. (f) Power distribution with different $Offset_Y$.

copper loss P_{cu2} in CH2 is only 5.9%, it is less than 1/10 of that in CH1, which is consistent with the theoretical values shown in Fig. 9(b). The power loss in CH2 accounts for only 8.3% of the total loss. It indicates that the proposed CH2 structure, which not only transmits part of the power but also serves as a control channel, introduces minimal additional power loss with negligible energy penalty.

Fig. 20 presents a comparative analysis of the proposed F3HDC-WPT system and a conventional SC-WPT system, both implemented on the same prototype, under various operating conditions including D variation and XY-axis misalignment.

In Fig. 20(a), the F3HDC-WPT system consistently achieves higher transmission efficiency than both SC-WPT with SPSC (single phase-shift control) and SC-WPT with PDM across a wide range of transmission power. Notably, the proposed system maintains efficiencies above 93% within a wide ZVS range. While the SC-WPT with PDM also achieves a wide ZVS range, its ZVS current approaches zero, which (due to the presence of parasitic capacitance) may still result in hard switching and partial energy loss. Consequently, its efficiency remains between that of the proposed F3HDC-WPT and the conventional SC-WPT with SPSC. Fig. 20(b) and (c) illustrates the system efficiency under X-axis and Y-axis misalignment, respectively. Even as misalignment increases, the F3HDC-WPT system maintains higher efficiency and a broader ZVS operating range compared to both SC-WPT methods.

Fig. 20(d) shows the corresponding active and reactive power distribution. As the duty cycle increases, the power contribution from CH2 also increases, accompanied by a moderate drop in CH2 reactive power Q_{CH2}, which helps maintain ZVS. Fig. 20(e) and (f) details the power distribution under these misalignment conditions. The active power is dynamically shared between CH1 and CH2, while CH2 also contributes adjustable reactive power Q_{CH2}, ensuring wide range ZVS.

D. Comparison of Existing Works

Table III compares the proposed F3HDC-WPT system with several existing methods in terms of efficiency, ZVS capability, control complexity, and coupler power density. The relatively high coupling coefficient (k) in CH1 results from the ZVS optimization design requirements, while the coupling coefficient in CH2 is comparable to or lower than the listed works. The proposed method achieves a high peak efficiency of 94.39% . Although this peak efficiency is comparable to some referenced studies, the proposed system clearly excels at partial loads, exhibiting a notably high half-power efficiency of 93.50% . Additionally, the proposed system provides a broader ZVS operation range compared to previous works, significantly enhancing efficiency, especially at partial load conditions. Furthermore, it achieves effective power control without communication devices or HFDS, reducing implementation costs and complexity.

In terms of power density, the proposed coupler achieves a moderate value (1.06 W/cm^2) compared with other methods, benefiting from its rational structural design. The introduction of the third harmonic channel does not significantly reduce the coupler's power density, indicating a well-balanced integration of harmonic transmission capability and physical compactness.

Although the proposed system adds an extra resonant channel and a ZCD-based sampling circuit, the overall cost increase is

TABLE III
COMPARISON OF EXISTING METHODS

Reference	[3]	[15]	[19]	[21]	[23]	[28]	[29]	[33]	This work
Power	0.5 kW	1 kW	3 kW	5 kW	1 kW	1 kW	0.13 kW	3 kW	1.7 kW
Dc Voltage Level	60 V	300 V	300 V	400 V	150 V	200 V	/	140 V	400 V
Switching Frequency	91.68 kHz	84.27 kHz	85 kHz	85.5 kHz	100+200 kHz	20 kHz	50 kHz	85 kHz	100 kHz
Resonant Frequency	91.68 kHz	84.27 kHz	85 kHz	85.5 kHz	100+200 kHz	18 kHz+54 kHz	50+150 kHz	85 kHz	100+300kHz
Coupling coefficient (k)	0.16~0.22	/	0.16—0.22	0.19—0.40	CH1: 0.30 CH2: 0.31	/	0.35—0.74	CH1:0.23 CH2:0.26	CH1:0.3—0.43 CH2:0.13—0.2
Peak Efficiency	94.19%	94.27%	91.5%	93.2%	84.1%	83%	83%	94%	**94.39%**
50% Power Efficiency	≈92%	<92.5%	/	≈90.0%	/	/	≈79%	/	**93.5%**
ZVS range	★	★	★★★	★★	/	/	★	★	★★★
Power Control Without Comm.	No	**Yes**	**Yes**	No	No	No	No	No	**Yes**
Without HFDS	No	**Yes**	**Yes**	**Yes**	/	/	/	/	**Yes**
Power Density of Couplers	/	/	0.65 W/cm^2	/	1.67 W/cm^2	/	0.80 W/cm^2	**2.14 W/cm^2**	1.06 W/cm^2
Cost Per Kilowatt Comparison	High	High	Low	Low	High	Medium	High	Low	Medium

Note: HFDS is high frequency digital sampling; Comm. is communication.

limited, as these additional components are low-cost compared to the overall system. As shown in Table III, the cost per kilowatt is estimated at a moderate level, reflecting a balanced tradeoff between added functionality and system cost.

Overall, the proposed topology offers superior efficiency, wide-range ZVS, simplified communication-free control, and balanced coupler performance, making it a competitive solution in practical WPT applications.

IV. CONCLUSION

This article has presented a novel F3HDC-WPT system, achieving closed-loop power control without communication devices or parameters identification techniques. Theoretical analysis of power transmission and comprehensive ZVS conditions was provided to validate the proposed system design. By introducing a harmonic channel and an efficient two-stage synchronous control strategy, the system simultaneously accomplishes communication-free closed-loop feedback and wide-range ZVS for all switches.

Experimental results confirmed that the proposed F3HDC-WPT system successfully realizes synchronous power regulation up to 1.7 kW, achieving a peak efficiency of 94.39% . Moreover, due to its wide-range ZVS capability, the system maintains high efficiency at partial loads, exhibiting approximately 93.5% efficiency at half-power conditions.

Compared to traditional single-channel WPT systems, the proposed F3HDC-WPT topology introduces an additional harmonic channel and corresponding control loop to achieve wide-range ZVS and communication-free power control. This inevitably increases system cost and control complexity. However, the overall control strategy remains relatively simple, and the loss introduced by the harmonic channel is shown to be minimal. Given these characteristics, the proposed method demonstrates promising potential for medium/high-power WPT applications.

In addition, the proposed design features a relatively short transmission distance and a correspondingly higher coupling coefficient. Future work may explore further optimization to enhance performance under lower coupling conditions, such as incorporating ferrite structures to extend transmission range, adopting more advanced topologies, and refining the design methodology.

Beyond the proposed S–S based topology, the proposed method also has potential to be applied in other compensation topologies such as *LCC*. While the *LCC* topology offers good constant-voltage output and better ZVS performance under load variations, its weaker current filtering makes it less suitable for the third harmonic phase feedback channel. However, using *LCC* in the fundamental channel could reduce the required third harmonic current for ZVS and improve performance under light load or frequent load changes. In such cases, the harmonic channel can still support power control under misalignment. Further investigation will be carried out in future work.

REFERENCES

[1] S. Li and C. C. Mi, “Wireless power transfer for electric vehicle applications,” *IEEE J. Emerg. Sel. Topics Power Electron.*, vol. 3, no. 1, pp. 4–17, Mar. 2015.

[2] Z. Zhang and H. Pang, “WPT for low-power applications,” in *Proc. Wireless Power Transfer, Princ. Appl.*, 2023, pp. 327–360.

[3] Y. Jiang, L. Wang, Y. Wang, J. Liu, X. Li, and G. Ning, “Analysis, design, and implementation of accurate ZVS angle control for EV battery charging in wireless high-power transfer,” *IEEE Trans. Ind. Electron.*, vol. 66, no. 5, pp. 4075–4085, May 2019.

[4] M. Yilmaz and P. T. Krein, “Review of battery charger topologies, charging power levels, and infrastructure for plug-In electric and hybrid vehicles,” *IEEE Trans. Power Electron.*, vol. 28, no. 5, pp. 2151–2169, May 2013.

[5] V.-B. Vu, V.-T. Phan, M. Dahidah, and V. Pickert, “Multiple output inductive charger for electric vehicles,” *IEEE Trans. Power Electron.*, vol. 34, no. 8, pp. 7350–7368, Aug. 2019.

[6] X. Liu, T. Wang, F. Gao, M. M. Khan, X. Yang, and D. J. Rogers, “A resonant inductor integrated-transformer-based receiver for wireless power transfer systems,” *IEEE Trans. Ind. Electron.*, vol. 70, no. 4, pp. 3616–3626, Apr. 2023.

[7] Z. Li, H. Liu, Y. Huo, J. He, Y. Tian, and J. Liu, “High-misalignment tolerance wireless charging system for constant power output using dual transmission channels with magnetic flux controlled inductors,” *IEEE Trans. Power Electron.*, vol. 37, no. 11, pp. 13930–13945, Nov. 2022.

[8] Y. Komiyama, A. Komanaka, W. Zhu, A. Konishi, K. Nguyen, and H. Sekiya, “Analysis and design of load-independent series resonant power amplifier with constant current output and its application for WPT system,” *IEEE Trans. Power Electron.*, vol. 39, no. 5, pp. 6515–6525, May 2024.

[9] X. Qu, Y. Yao, D. Wang, S.-C. Wong, and C. K. Tse, “A Family of hybrid IPT topologies with near load-independent output and high tolerance to pad misalignment,” *IEEE Trans. Power Electron.*, vol. 35, no. 7, pp. 6867–6877, Jul. 2020.

[10] A. Kuperman, "Simple enhancement of series–Series-compensated inductive wireless power transfer links operating with load-independent voltage output at fixed frequency to attain zero inverter phase angle," *IEEE Trans. Power Electron.*, vol. 38, no. 5, pp. 5670–5674, May 2023.

[11] W. Zhong and S. Y. R. Hui, "Charging time control of wireless power transfer systems without using mutual coupling information and wireless communication system," *IEEE Trans. Ind. Electron.*, vol. 64, no. 1, pp. 228–235, Jan. 2017.

[12] J. Heo, S.-W. Kim, I.-K. Cho, I. Ju, and Y. B. Park, "Power distribution control method in communication–Free MIMO–WPT through load impedance and mutual inductance estimation," *IEEE Access*, vol. 12, pp. 78825–78832, 2024.

[13] R. Bosshard, J. W. Kolar, and B. Wunsch, "Control method for inductive power transfer with high partial-load efficiency and resonance tracking," in *Proc. Int. Power Electron. Conf.*, 2014, pp. 2167–2174.

[14] P. Pham, S. Cochran, D. J. Costinett, and L. M. Tolbert, "Active rectifier design and synchronization control for 6.78 MHz wireless power transfer," in *Proc. IEEE Energy Convers. Congr. Expo.*, 2020, pp. 5501–5508.

[15] D. Zhang, M. Chen, B. Li, X. Wang, X. Sun, and F. Jiang, "A synchronization strategy based on resonant current detection for bidirectional wireless charging system," *IEEE Trans. Power Electron.*, vol. 37, no. 9, pp. 11436–11449, Sep. 2022.

[16] S. Zhao, Y. Li, D. Wu, and R. Mai, "Current-decomposition-based digital phase synchronization method for BWPT system," *IEEE Trans. Power Electron.*, vol. 36, no. 11, pp. 12183–12188, Nov. 2021.

[17] X. He et al., "Wireless power and information dual transfer system via magnetically coupled resonators," *Commun. Eng.*, no. 8, pp. 1–12, Mar. 2024.

[18] S. Cochran and D. Costinett, "Discrete time synchronization modeling for active rectifiers in wireless power transfer systems," in *Proc. 20th Workshop Control Model. Power Electron.*, 2019, pp. 1–8.

[19] Z. Luo, Y. Zhao, M. Xiong, X. Wei, and H. Dai, "A self-tuning LCC/LCC system based on switch-controlled capacitors for constant-power wireless electric vehicle charging," *IEEE Trans. Ind. Electron.*, vol. 70, no. 1, pp. 709–720, Jan. 2023.

[20] J. Tang, T. Na, and Q. Zhang, "A novel full-bridge step density modulation for wireless power transfer systems," *IEEE Trans. Power Electron.*, vol. 38, no. 1, pp. 41–45, Jan. 2023.

[21] X. Li, D. Zhou, S. Jia, X. Liu, and J. Zou, "A WPT system with wide-range voltage gains and soft switching via primary-side hybrid modulation," *IEEE Trans. Power Electron.*, vol. 39, no. 7, pp. 8985–8997, Jul. 2024.

[22] C. Xia, N. Wei, H. Zhang, S. Zhao, Z. Li, and Z. Liao, "Multifrequency and multiload MCR-WPT system using hybrid modulation waves SPWM control method," *IEEE Trans. Power Electron.*, vol. 36, no. 11, pp. 12400–12412, Nov. 2021.

[23] Y. Liu, C. Liu, X. Gao, and S. Liu, "Design and control of a decoupled multichannel wireless power transfer system based on multilevel inverters," *IEEE Trans. Power Electron.*, vol. 37, no. 8, pp. 10045–10060, Aug. 2022.

[24] H. Zhang and Y.-X. Deng, "High-isolated wireless power and information codelivery by exploiting backscattered second harmonics," *IEEE Antennas Wireless Propag. Lett.*, vol. 23, no. 5, pp. 1538–1542, May 2024.

[25] S. D. Joseph, Y. Huang, S. S. H. Hsu, A. Alieldin, and C. Song, "Second harmonic exploitation for high-efficiency wireless power transfer using duplexing rectenna," *IEEE Trans. Microw. Theory Techn.*, vol. 69, no. 1, pp. 482–494, Jan. 2021.

[26] C. Xia et al., "Inductive power and signal synchronous transmission based on parallel paths of fundamental wave and harmonic wave," *Automat. Electric Power Syst.*, vol. 42, no. 5, pp. 169–175, Mar. 2018.

[27] Y. Li et al., "Research on hybrid dual-frequency IPT system against misalignment with constant output voltage," in *Proc. Chin. Soc. Elect. Eng.*, Sep. 2022, pp. 1–10.

[28] H. Zeng, S. Yang, and F. Z. Peng, "Design consideration and comparison of wireless power transfer via harmonic current for PHEV and EV wireless charging," *IEEE Trans. Power Electron.*, vol. 32, no. 8, pp. 5943–5952, Aug. 2017.

[29] W. Xiong et al., "A dual-frequency-detuning method for improving the coupling tolerance of wireless power transfer," *IEEE Trans. Power Electron.*, vol. 38, no. 6, pp. 6923–6928, Jun. 2023.

[30] C. Luo, D. Qiu, W. Gu, B. Zhang, Y. Chen, and W. Xiao, "Multiload wireless power transfer system with constant output power and efficiency," *IEEE Trans. Ind. Appl.*, vol. 58, no. 1, pp. 1101–1114, Jan./Feb. 2022.

[31] W. McMurray, "Selection of snubbers and clamps to optimize the design of transistor switching converters," *IEEE Trans. Ind. Appl.*, vol. IA-16, no. 4, pp. 513–523, Jul. 1980.

[32] J. Wu, T. Wang, Z. Shu, L. Ma, S. Wang, and J. Nie, "Power balance control based on sensorless parameters estimation for ISOP three-level DAB converter," *IEEE Trans. Ind. Electron.*, vol. 71, no. 10, pp. 12414–12424, Oct. 2024.

[33] M. Wu et al., "A compact coupler with integrated multiple decoupled coils for wireless power transfer system and its anti-misalignment control," *IEEE Trans. Power Electron.*, vol. 37, no. 10, pp. 12814–12827, Oct. 2022.